Journal of The Electrochemical Society

OPEN ACCESS

Effects of Pore Structure and Carbon Loading on Solid Capacitive Devices at Low Temperatures

To cite this article: Alvin Virya *et al* 2022 *J. Electrochem. Soc.* **169** 070522

Journal of The Electrochemical Society, 2022 **169** 070522

Effects of Pore Structure and Carbon Loading on Solid Capacitive Devices at Low Temperatures

Alvin Virya,[*,z] Raunaq Bagchi,[*] and Keryn Lian[**]

Department of Materials Science and Engineering, University of Toronto, Toronto, Ontario M5S 3E4, Canada

The effects of electrode material loading and operating temperature on solid-state electrochemical double layer capacitors (EDLCs) with Na_2SO_4-polyacrylamide-DMSO electrolyte were studied. Two types of solid EDLC cells, using carbon nanotube (CNT) or activated carbon (AC), with very different surface areas and pore structures were compared to reveal the limitations in designing solid capacitive devices. Based on the gravimetric capacitance values, the utilizable portion of the electrode for EDLC can be estimated. Although increasing carbon loading leads to higher capacitance, there are two possible adverse effects especially at low temperatures. A high loading and thick electrode may reduce the penetration of viscous polymer electrolyte precursor solutions and may increase diffusion limitation leading to lower material utilization. These phenomena are more aggravated at faster rates and on micropore-rich materials. The results from this work can be used to quantify the effective utilization of the materials at different temperatures and the insights can be added to the guiding principles for designing and developing solid EDLCs.

 [DOI: 10.1149/1945-7111/ac7ef1]

Manuscript submitted May 2, 2022; revised manuscript received June 22, 2022. Published July 20, 2022. *This paper 1285, was presented during the 240th Meeting of the Electrochemical Society, October 10–14, 2021.*

Supplementary material for this article is available online

Polymer electrolytes are the key enablers for safe, thin, flexible, and solid-state electrochemical capacitors (ECs) that can power emerging wearable electronics and Internet-of-Things devices.[1,2] Many polymer electrolytes, functioning as both ion conductors and separator, have been reported for their high ionic conductivity, good processability, and environmental stability in recent years.[2–6] Aqueous-based neutral pH polymer electrolytes are particularly promising for their wider cell voltage window over proton- or hydroxide ion-conducting counterparts,[7–10] due to their high overpotential of water decomposition reactions.[11–13] One such example is a ternary polymer electrolyte comprising of Na_2SO_4 ion conductor, polyacrylamide (PAM) host, and dimethyl sulfoxide (DMSO) additive, referred to as Na_2SO_4-PAM-DMSO. This polymer electrolyte has several desirable characteristics: high ionic conductivity of ca. 30 mS cm^{-1} at ambient temperature, wide 1.8 V window with carbon electrodes, and stable performance across long shelf-life (>30 d) and wide temperature range (−20 °C to +80 °C).[14]

The next generation ECs will have a wide variety of forms with each individual recommended electrode thickness depending on the specific application, e.g., 100 μm in practical EDLCs with liquid electrolytes,[15] 1–100 μm for flexible electronics[16,17] or <50 μm in microelectrodes[18]; but these standards may not be directly applicable in polymer electrolytes-based EDLCs. To apply polymer electrolytes to solid ECs, in addition to the same practices in liquid devices (e.g., matching of electrolytes to the chemistry and pore size/structures of electrodes, operating conditions, cell configurations, etc.[15,19–25]), their viscous nature of precursor solutions must also be considered (e.g., ca. 9,000 vs <1 cP in precursor solution of Na_2SO_4-PAM-DMSO vs 0.5 M Na_2SO_4 solution). This effect is more noticeable when applying polymer electrolytes to those electrodes possessing small and tightly-closed pore structures (e.g., commercial YP-50 activated carbon (AC)).[26] This was demonstrated by a systematic study on 2 different ACs with 3 polymer electrolytes at different loadings and compared to their respective liquid counterparts by Wu et al.[27]

The development of solid ECs that can function at sub-zero temperatures is challenging but important for applications in sub-polar climates or outdoor winter environments.[20,28,29] At low temperatures, the electrode utilization can be even more limited, not only from lower electrolyte accessibility but also from the greatly reduced conductivities of the electrolytes.[29] For example, in Na_2SO_4-PAM-DMSO, the ionic conductivity decreased from 19 mS cm^{-1} at +20 °C to 0.2 and 0.02 mS cm^{-1} at −10 and −20 °C respectively,[30] which can significantly impact the operation of the solid devices at low temperatures. Thus, it is of fundamental and practical importance to quantify the effective electrode loading for different types of carbon material at low temperatures and compare them to their respective baselines at ambient. Although the ternary Na_2SO_4-PAM-DMSO electrolytes were functional in solid ECs with carbon nanotubes (CNT) electrodes at as low as −20 °C, the loading of the active material was low and might not reflect the maximum performance.[14]

In this work, a systematic study of Na_2SO_4-PAM-DMSO electrolytes on 2 carbon materials with different pore structures and surface areas was performed using solid ECs to reveal the insights on effective loading at ambient and low temperatures. Two case studies were conducted based on 2 known commercial carbon materials: (1) CNT with mostly open mesopores (pore sizes ranging between 10 and 100 nm size[31,32]) and but small specific surface area (SSA) of ca. 100 m^2 g^{-1}, and (2) YP-50 AC that has high SSA of 1,700 m^2 g^{-1} but containing mainly small and closed micropores.[27] By comparing the cell performance using these two carbon materials, the effective electrode utilization can be estimated to reveal the influences of temperature and electrode pore structure on the solid EC performance.

Experimental

Preparation and characterization of polymer electrolyte.—The preparation of the Na_2SO_4-PAM-DMSO electrolyte has been described in a previous report.[30] On a dry weight basis, the polymer electrolytes comprised of 16, 62, and 22 wt% of Na_2SO_4, PAM, and DMSO, respectively; corresponding to a molar ratio between Na_2SO_4:PAM:DMSO of 10,000:1:25,000. The precursor solutions were prepared by mixing an aqueous solution containing 3 wt% PAM (Scientific Polymer Products, Mw 5,000,000–6,000,000) with Na_2SO_4 (Alfa Aesar, ACS >99%) and DMSO (Alfa Aesar) and stirred for 3–4 d. PAM with high molecular weight was chosen as the polymer host for its chemical compatibility with Na_2SO_4, high water retention, and ability to form a mechanically stable polymer electrolyte.

The thermal properties of the ternary electrolytes were studied using differential scanning calorimetry (DSC). To prepare the DSC

*Electrochemical Society Student Member.
**Electrochemical Society Member.
[z]E-mail: alvin.virya@utoronto.ca

samples, electrolyte precursor solutions were directly cast onto a pan (Tzero™ hermetic pan) and let water evaporate. The pans were sealed using a hydraulic press when the sample reached a water content of 70 wt%, mimicking the pristine electrolyte in an electrochemical test cell. The thermal diagrams were recorded on TA instrument Q2000 system, between −30 °C and +20 °C with a scan rate of 2 °C min^{-1}, under N_2 atmosphere.

Electrode fabrication.—The preparations of the CNT-graphite[33] and YP-50 AC[34] electrodes were described in previous reports. Both carbon materials were selected from commercial sources with good consistency and highly uniform structures that allow for fair and systematic comparison among various cells under different test conditions. The CNT-graphite electrodes consisted of 60 wt% multi-walled CNT (MWCNT), 20 wt% graphite, and 20 wt% crosslinked PVA binder. Briefly, MWCNT (Cheap Tubes Inc., partially graphitized with outer diameters of 10–20 nm), graphite (Alfa Aesar), and glutaric acid as crosslinker were added into 5 wt% aqueous solution of PVA (Alfa Aesar, Mw of 145,000) and stirred as slurry over several days. The CNT electrodes were prepared by casting the water-based slurry onto titanium current collector and left to dry followed by curing at 120 °C for 1 h. The loadings of CNT electrodes ranged from 0.8 (thin), 3.1 (medium), to 6.4 mg cm^{-2} (thick). The variation in CNT loading was achieved by adjusting the wet thickness coated (Table I), leading to the thickness of the dry electrodes from 60 (thin) to 150 μm (thick).

The AC electrodes consisted of 85 wt% AC, 5 wt% carbon black, and 10 wt% poly(vinylidene fluoride) (PVDF) binder. An NMP-based slurry containing AC (Kuraray YP-50), carbon black (Alfa Aesar), and PVDF (Arkema Kynar HSV900) binder was stirred overnight. PVDF is used as binder for its better material compatibility and film formability with YP-50 AC. The slurry was also deposited onto titanium current collector and dried at 120 °C. Electrodes with two loadings of YP-50 AC were constructed containing either 0.8 (thin) or 3.0 mg cm^{-2} (medium) active material loading. The thin electrode was achieved by diluting YP-50-containing slurry with NMP solvent from its regular formulation (see Table II). Once the electrodes were dried, the coated thicknesses were ca. 28 (thin) and 52 μm (medium), respectively.

Solid EC cells assembly and electrochemical characterizations.—Both types of solid EC cells had an apparent area of 1 cm^2. The solid cells were assembled by casting the electrolyte precursor solution onto each electrode followed by sandwiching the semi-dried electrolyte between the two electrodes and protecting it with tape. The thickness of these cells was measured using a Mitutoyo digital micrometer; the total cell thickness was between 0.6–0.7 mm with a 0.2–0.3 mm thick electrolyte.

All cells were characterized using cyclic voltammetry (CV) and electrochemical impedance spectroscopy (EIS) at temperatures between −20 and +20 °C inside an environmental chamber (ESPEC SH-241). The cells were acclimated at each tested temperature for 1 h before measurement. The electrochemical measurements were conducted using EG&G Princeton Applied Research 263 A potentiostat/galvanostat interfaced with a Solartron 1255 frequency response analyzer. The cell capacitance (C_{cell}) from CV was calculated via Eq. 1, through dividing the charge (Q) by the cell potential window (V):

$$C_{cell} = \frac{Q}{V} \quad [1]$$

The CVs were recorded with various scan rates, ranging from 10 mV s^{-1} to 10 V s^{-1} for CNT cells, and from 1 mV s^{-1} to 5 V s^{-1} for AC cells. To estimate the gravimetric capacitance (C_{grav}) of a single electrode, the cell capacitance (C_{cell}) was normalized against the average weight of carbon materials from both electrodes (m_C) (Eq. 2):

$$C_{grav} = \frac{2 \times C_{cell}}{m_C} \quad [2]$$

EIS spectra were recorded from 100 kHz to 0.1 Hz (for CNT cells) or to 0.01 Hz (for AC cells). The frequency-dependent complex capacitance can be deconvoluted into real and imaginary components via Eqs. 3 and 4, respectively:

$$C' = \frac{Z''}{(2\pi f)\ |z|^2} \quad [3]$$

$$C'' = \frac{Z'}{(2\pi f)\ |Z|^2} \quad [4]$$

where the Z' and Z'' are the real and imaginary components of impedance and f is the frequency in Hz. The real component C' corresponds to the amount of accessible charge in a capacitor, whereas the imaginary capacitance C'' signifies the energy dissipation of the device.[35] The values of C' and C'' from single electrodes were normalized to the weight of carbon materials using Eq. 2, similar to the DC response counterpart.

Results and Discussion

The influence of temperature and active material loading on CNT (Case-1) and YP-50 (Case-2) were studied by analyzing the capacitance and rate capability for their respective solid cells. In addition to their differences in surface area and pore size distribution, CNT possesses higher electronic conductivity due to the higher portion of graphitic carbon than AC as reflected by almost double the I_D/I_G ratio in the Raman spectra (Fig. S1a (available online at stacks.iop.org/JES/169/070522/mmedia)). Nevertheless, the effects from such differences were negligible when compared to the expected decrease in ionic conductivity at low temperatures. On the other hand, both YP-50 AC and CNT contain mostly carbon

Table I. List of CNT electrodes with varying carbon loading.

Active Materials	Wet Slurry Thickness (μm)	Carbon Loading (mg cm^{-2})	Electrode Label
MWCNT (*SSA: 100 m^2 g^{-1}*) 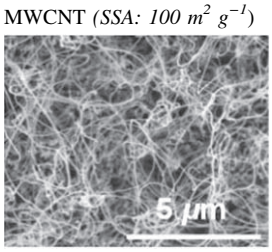	400	0.8	Thin
	800	3.1	Medium
	1,000	6.4	Thick

Table II. List of YP-50 AC electrodes with varying carbon loading.

Active Materials	Wet Slurry Thickness (μm)	Carbon Loading (mg cm^{-2})	Electrode Label
YP-50 AC *(SSA: 1,700 m^2 g^{-1})* 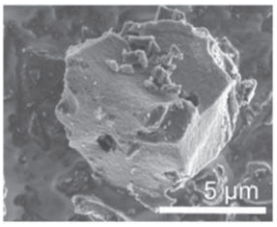	100 (3 × dilution)	0.8	Thin
	100	3.0	Medium

with small variation in the oxygen-containing quinone group (in Fig. S1b). However, the pseudocapacitive contributions of the quinone groups are relatively minimal in a neutral pH environment and both carbons can be well-wetted with PAM-based electrolytes.[9,14,27] Thus, the results from these two carbons can be used to estimate the effective electrode utilization and to reveal the impact of electrode pore structure on device performance at different temperatures.

Case-1: solid devices with various CNT loadings.—CV study on solid cells with 3 different CNT loadings was conducted at +20, −10, and −20 °C. Figs. 1a to 1c were obtained at the slow scan rate of 10 mV s^{-1}, while Figs. 1d to 1f were acquired at the faster rate of 100 mV s^{-1}. At a slow rate of 10 mV s^{-1}, the capacitive CV profiles and gravimetric capacitance of the cells with thin (black curves) and medium electrodes (blue curves) were similar at all 3 temperatures, suggesting a comparable material utilization. Although the ionic conductivity of Na_2SO_4-PAM-DMSO electrolyte was considerably lower (retaining only 10 and 1% respectively at −10 and −20 °C), it had a relatively negligible effect on these lower loading electrodes. On the other hand, the CVs of the cells with thick CNT electrodes (red curves) showed lower gravimetric current at all 3 temperatures, indicating a lower material utilization.

At a higher rate of 100 mV s^{-1} (Figs. 1d to 1f), the rate capability of these devices deteriorated with decreasing temperatures due to the significant loss of ionic conductivity. For example, while all cells exhibited highly rectangular profiles at +20 °C (Fig. 1d), none were able to maintain the rectangular CV profile at −20 °C (Fig. 1f). The degradation in rate performance was more aggravated with thicker electrodes when comparing the CVs at −10 °C (Fig. 1e), where the cells having thick CNT electrodes were mostly resistive.

The areal capacitances of these devices were calculated from the CVs and plotted as a function of scan rates in Figs. 2a to 2c. Under ambient conditions, the capacitance was proportional to the loadings of the active materials at low scan rates (Fig. 2a) but deviated at higher scan rates. At 10,000 mV s^{-1}, the cells having the thick electrodes retained only 29.4% of the capacitance at 10 mV s^{-1}, below the 71.6 and 55.6% from those of thin and medium electrodes. This is expected from their longer time constants ($\tau = RC$) of the devices that have higher capacitance. The slower response translates into a poorer rate performance, which results in less rectangular CVs and lower deliverable capacitance of devices with increased

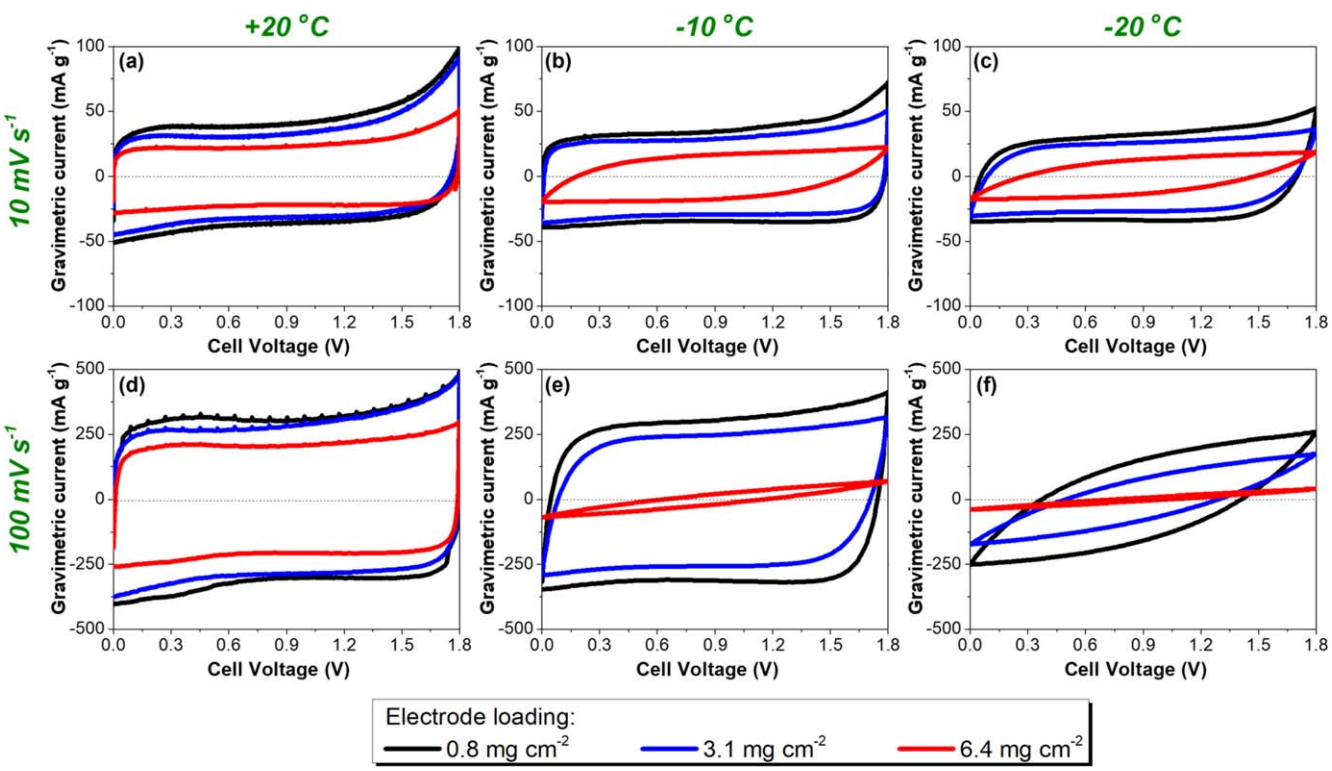

Figure 1. CVs of CNT cells with various electrode loading using 10 mV s^{-1} scan rate (top) at (a) +20, (b) −10, and (c) −20 °C; and using 100 mV s^{-1} rate (bottom) at (d) +20, (e) −10, and (f) −20 °C. The current responses were normalized to the weight of CNT.

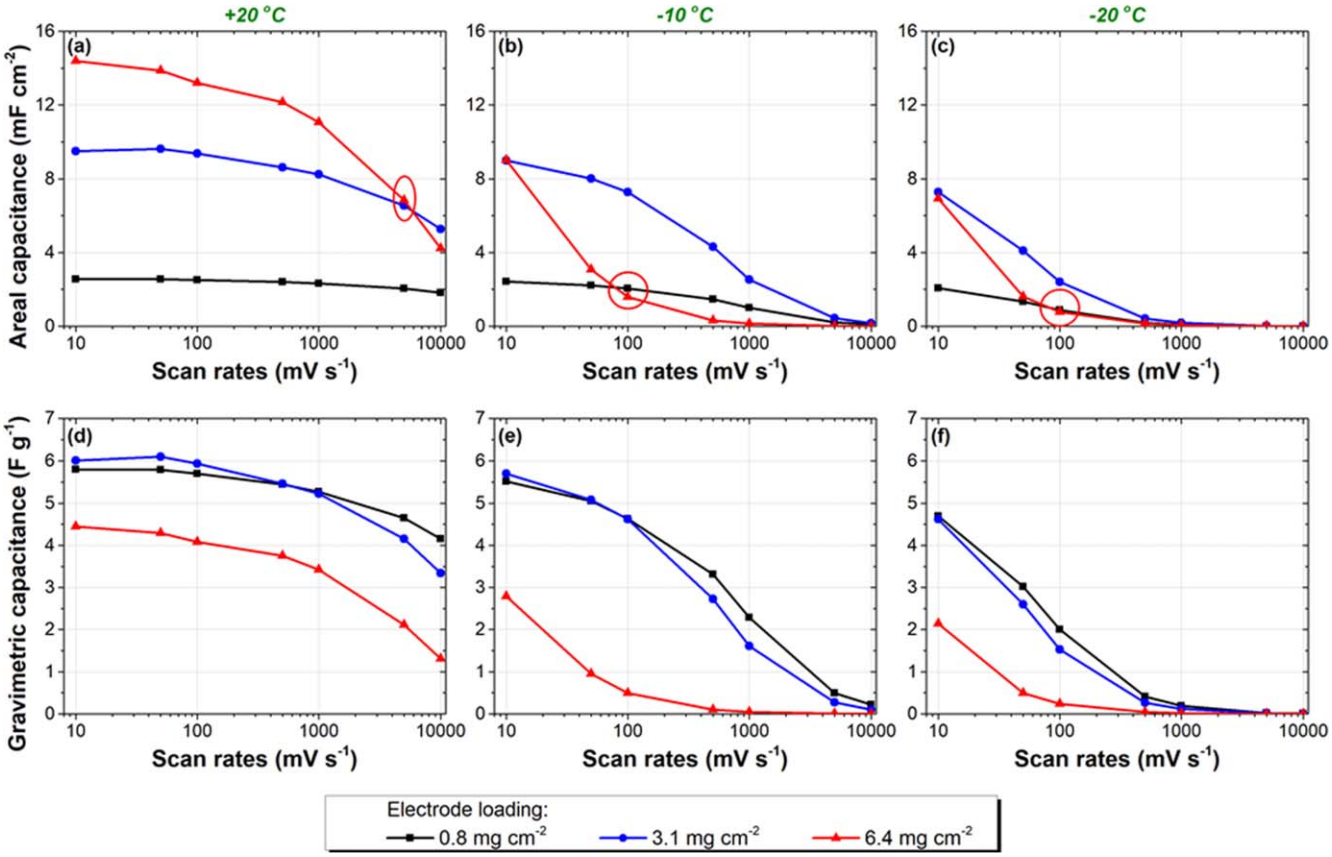

Figure 2. Capacitance of CNT cells in various scan rates normalized with apparent area (top, red circles indicate crossover points in areal capacitance) at (a) +20, (b) −10, and (c) −20 °C; and normalized to the carbon loading (bottom) at (d) +20, (e) −10, and (f) −20 °C.

electrode loading at faster scan rates. On the other hand, at sub-zero temperatures (Figs. 2b and 2c), there was little difference in capacitance between the devices with medium and thick electrodes at 10 mV s^{-1}, implying a significant portion of unutilized active material on the thick electrode. These under-utilized electrodes resulted in the lower gravimetric capacitance across all 3 temperatures (red lines in Figs. 2d to 2f). At +20 °C, despite having higher capacitance on the areal basis, the device with thicker electrodes showed lower gravimetric capacitance which suggests significantly lower electrode utilization. This effect is worsened at lower temperatures due to the sluggish movement of ions, especially at sub-zero temperatures.

The unutilized portion of the thicker electrodes resulted in waste of materials, poor rate performance, and high cell resistance under sub-zero temperatures. In Figs. 2a to 2c, the areal capacitances of devices with thick electrodes are worse than those containing thinner electrodes at higher scan rates. The Nyquist plots (Figs. S2a to S2c in appendix) also revealed that, while the cells with thin and medium electrodes remained highly capacitive even at −20 °C, those cells with thick electrodes showed significantly higher interfacial polarization resistance as shown through the larger semi-circles at sub-zero temperatures. Using the scan rate-dependent gravimetric capacitance values from Figs. 2d to 2f, Trasatti's method was applied to deconvolute the capacitance into their pure EDL and diffusion-limited component.[36] Through this approach, the maximum capacitance value, reflecting the theoretical maximum capacitance at slow scan rate approaching zero (C_0), was estimated by interpolating the plot of inverse of capacitance (1/C) against the square-root of scan rate ($\nu^{0.5}$) in Fig. S3a. Meanwhile, the pure EDL component can be estimated using the theoretical capacitance values at infinitely large scan rates (i.e., C_∞ which represents pure EDL component) through interpolation of the capacitance value (C) against the inverse-square-root of scan rate ($\nu^{-0.5}$) (Fig. S3b). The deconvolution revealed that the capacitances were mostly pure EDL component but with increased portion of diffusion-limited capacitance with carbon loading (Figs. S3c and S3d for +20 and −10 °C). As a result, there are some crossover points (circled in each figure) where additional active materials no longer contribute any capacitance at the fast rates (e.g., between medium and thick electrodes at 500 mV s^{-1}). A similar observation was also seen on the frequency-dependent complex capacitance in Fig. 3. The time constant τ, derived from the peak in imaginary capacitance (C')-frequency curve in Fig. 3a, was 0.8 s for the thick electrode, much longer than 0.15 and 0.06 s in the medium and thin electrodes at +20 °C. At the sub-zero temperatures (Figs. 3b and 3c), while cells having thin and medium electrodes began to be capacitive at 0.01 Hz, those with thick electrodes remained close to their resistance-dominated state—consistent with the trend in their DC responses in Fig. 1.

Case-2: solid devices with various YP-50 AC electrode loadings.—Similar analysis was conducted on a commercial YP-50 AC that has smaller pores (primarily between 1–2 nm size) and a more closed pore structure. The CVs at all 3 temperatures are displayed in Figs. 4a to 4c for slow scan rate of 1 mV s^{-1} and in Figs. 4d to 4f for the faster rate of 10 mV s^{-1}. Both thin (black curves) and medium electrodes (blue curves) had similar CV profiles at 20 °C in Figs. 4a and 4d. The resulting gravimetric capacitance of the medium electrodes is slightly less than those with thin electrodes (i.e., 75 vs 87 F g^{-1}), due to the lower infiltration of the electrolyte precursor solution as reported by Wu et al.[27]

Some of the observations from CNT cells were also seen in AC cells: less rectangular CVs at lower temperatures than those at ambient (e.g., Figs. 4c vs 4a), and reduced rate capability with the increase of active material loading. Nevertheless, the threshold loading that triggered resistive performance at sub-zero temperatures is significantly lower in loading for YP-50 AC. Using Trasatti's

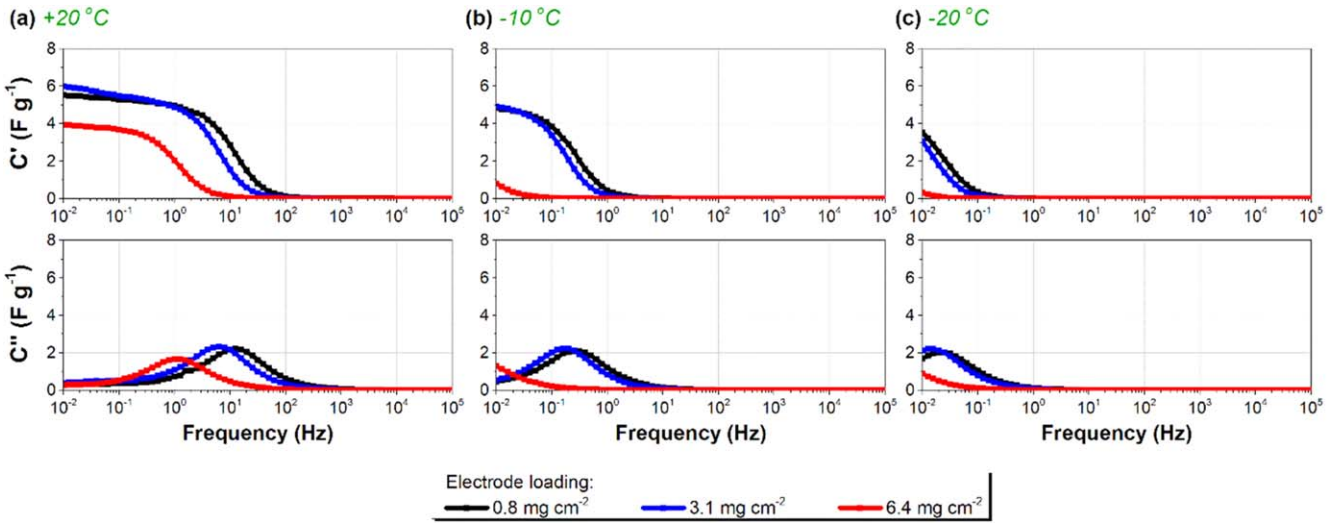

Figure 3. Frequency-dependent complex capacitance (real C' and imaginary C' on the top and bottom, respectively) calculated from EIS on solid CNT cells at (a) +20, (b) −10, and (c) −20 °C.

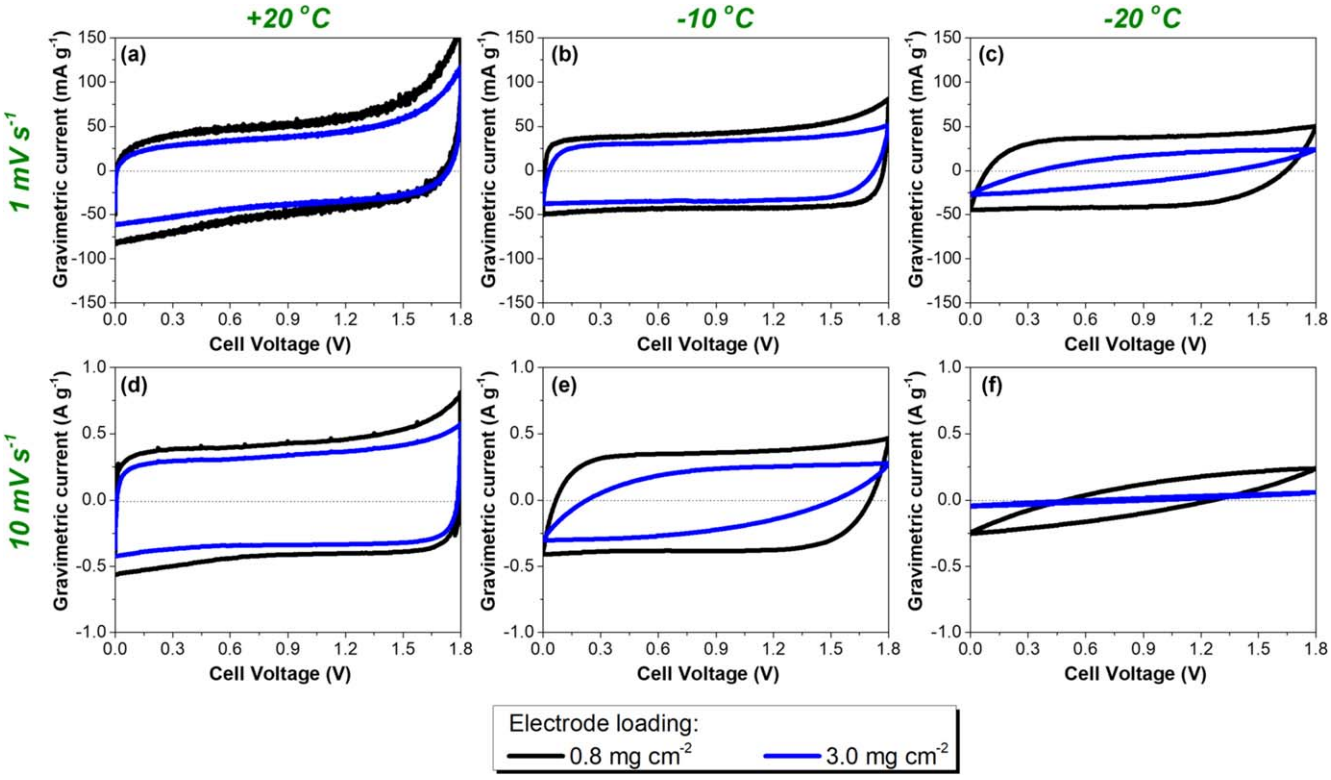

Figure 4. CVs, normalized to the weight of active materials, obtained from YP50-based EDLCs with various electrode loading using 1 mV s^{-1} scan rate (top) at (a) +20, (b) −10, and (c) −20 °C; and using 10 mV s^{-1} rate (bottom) at (d) +20, (e) −10, and (f) −20 °C.

analysis to deconvolute the capacitance (Figs. S4a and S4b), a >20% of diffusion-limited portion was obtained at +20 °C (Fig. S4c), likely from the tortuous ion path through the closed pore structure of YP-50 AC. Consequently, the medium loading of ca. 3.0 mg cm^{-2}, the CV profile became more resistive on AC electrodes even at a slower rate of 1 mV s^{-1} in Figs. 4a and 4b compared to CNT with the same loading at a higher rate (Figs. 1a and 1b). The reduction in the rate capability from higher carbon loading or lower temperature was quantified through their frequency-dependent complex capacitances (Figs. 5a to 5c) and related Nyquist plots (Fig. S5). The cells having thick electrodes exhibited slower frequency response across all 3 tested temperatures. At +20 °C, this trend was expected as the higher loading increased the overall capacitance and a greater τ (Fig. 5a). Meanwhile, at −20 °C where the ESR is much higher compared to that at +20 °C (3,000–4,000 Ω cm^2 vs 2.5 Ω cm^2, from Figs. S5a and S5c), both cells could barely enter the capacitive state even at 0.01 Hz (τ >100 s, shown in the inset to Fig. 5c). This observation is consistent with the non-rectangular CV profiles at 10 mV s^{-1} at the same temperature in Fig. 4f.

The areal capacitances of both YP-50 cells were plotted as a function of scan rates at all 3 temperatures (Figs. 6a to 6c). At +20 °C, the capacitance of cells with medium-loading electrodes was 112.2 mF cm^{-2} at low scan rate (Fig. 6a), almost 3 × of those of the thin electrodes (38.1 mF cm^{-2}). However, this gap diminished at

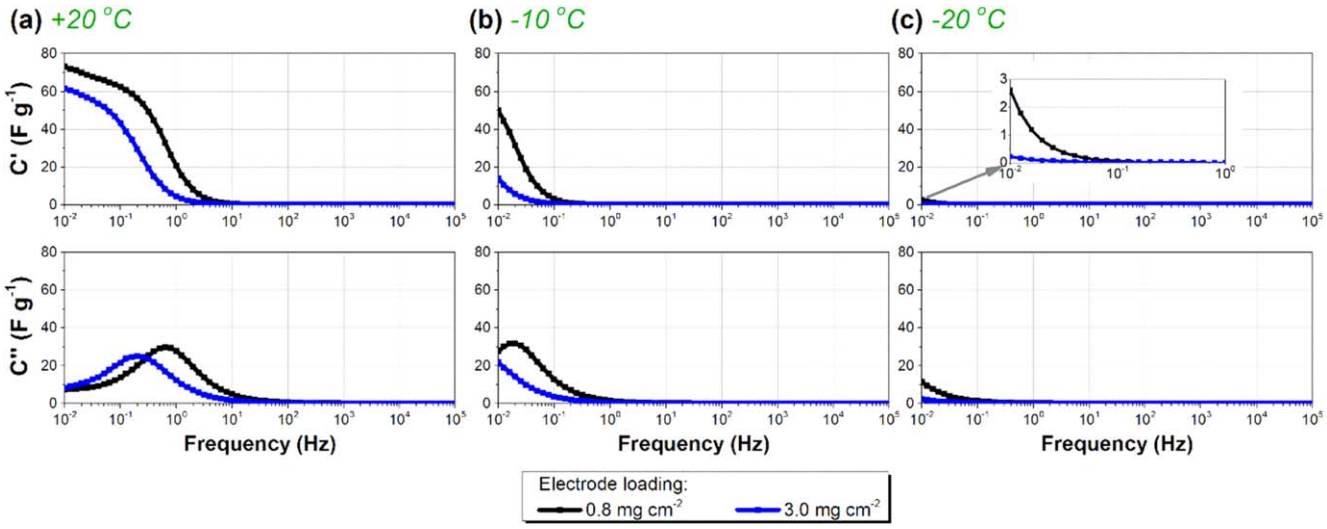

Figure 5. Frequency-dependent complex capacitance (real C' and imaginary C' on the top and bottom, respectively) calculated from EIS on solid YP-50 cells at (a) +20, (b) −10, and (c) −20 °C.

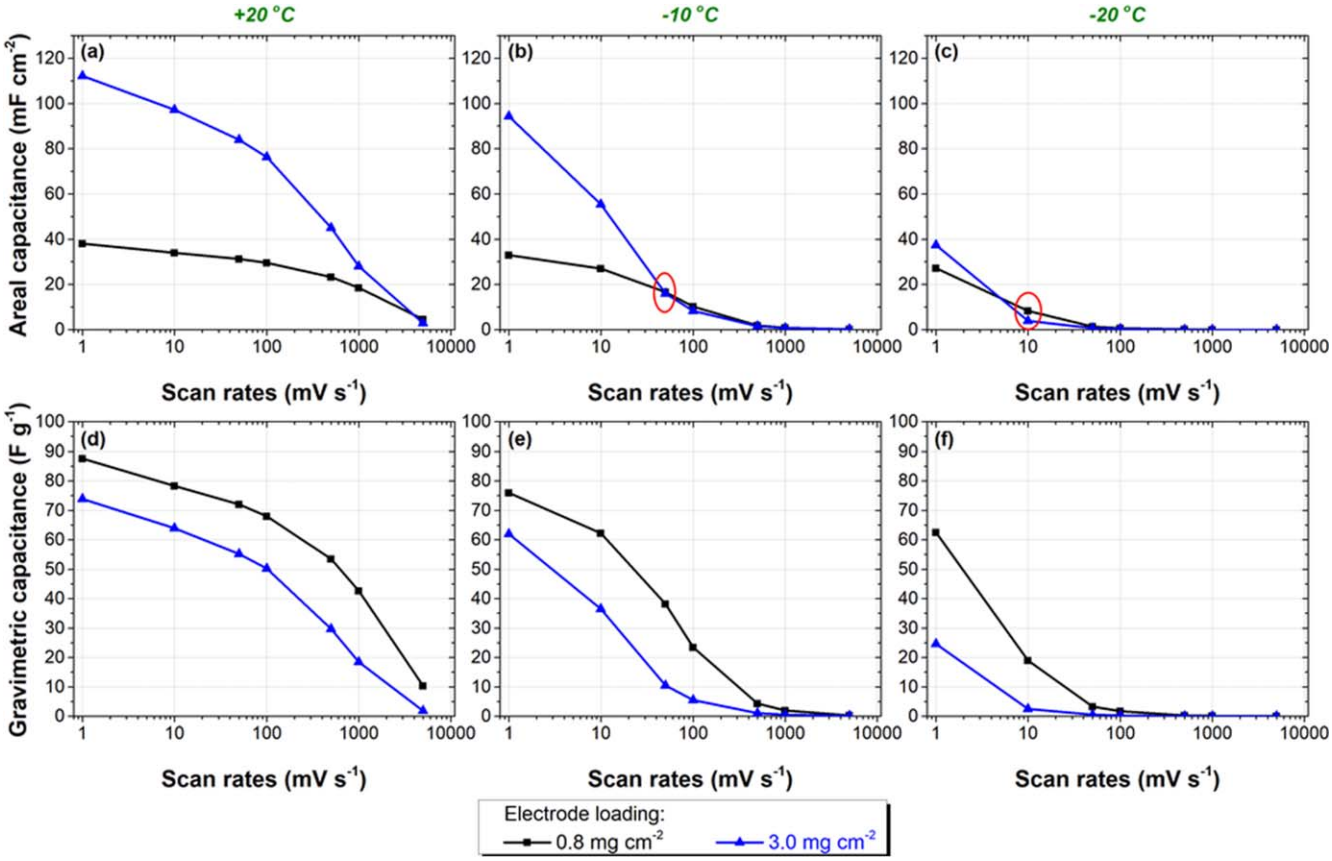

Figure 6. Capacitance of YP-50 cells in various scan rates normalized with area (top) at (a) +20, (b) −10, and (c) −20 °C; and normalized with carbon loading (bottom) at (d) +20, (e) −10, and (f) −20 °C.

−20 °C, where the areal capacitance of the medium electrode-containing cells was only slightly higher than that with thin electrode (37.4 vs 27.2 mF cm^{-2}, Fig. 6c). This implies that there was significantly more unutilized material that no longer contributes to deliverable capacitance in the thicker electrode at −20 °C, leading to the lower gravimetric capacitance in Figs. 6d to 6f.

Comparison of CNT vs AC in Na_2SO_4-PAM-DMSO at low temperatures.—From the two case studies of Na_2SO_4-PAM-DMSO with different carbon materials, the maximum active materials loadings, usable capacitance, and their rate performance in solid EDLCs are strongly influenced by the SSA, pore structure, and operating temperature. There is a need to balance the benefit of higher capacitance between the loading of active materials and the performance (rate, temperature, etc). Through the comparison of their capacitive behavior from ambient to low temperatures, the actual utilization of these two carbon electrodes can now be quantified.

One way to explore these differences is to normalize the gravimetric capacitance at low temperatures by their respective baselines at +20 °C, where the maximum capacitance was reached. The comparisons of these capacitance retentions at low temperatures at different loadings are shown in Fig. 7a for CNT and 7b for YP-50 AC. In both cases, the capacitance retained at low-loading electrodes (grey bar, at 0.8 mg cm^{-2}) remained high, suggesting full utilization at all temperatures despite the reduction in ionic conductivities of the Na_2SO_4-PAM-DMSO electrolytes. High capacitance retention can still be achieved at medium electrode loading in CNT cells, but not in those with YP-50 AC electrodes with the same 3 mg cm^{-2} loading (cyan bar), especially at −20 °C. This implies a severe under-utilization of the electrode materials at low temperatures in AC, even though the thickness of YP-50 AC electrodes is only half of the CNT electrode at comparable mass loading (52 vs 103 μm for medium loading). These findings strongly suggest that the optimal thickness can vary significantly depending on the pore accessibility of the electrode materials. The under-utilization of electrodes was only observed in very heavy/thick CNT electrodes (e.g., 6.5 mg cm^{-2}, 150 μm thick, magenta bar).

So far, the evidence showed a strong influence from carbon loading on electrode utilization, but the effects of electrolyte properties must also be considered. The thermal property of the Na_2SO_4-PAM-DMSO electrolyte was characterized using DSC and revealed a melting peak below −10 °C. The DSC curve was overlaid with the ionic conductivities in Fig. 8 together with the electrode utilization estimated on all tested temperatures. The percentages of electrode utilization obtained from their gravimetric capacitances at the low scan rates, under the assumption that low-loading electrodes of 0.8 mg cm^{-2} in Figs. 2 and 4 are fully utilized at +20 °C. These three tested temperatures also reflected the situations at ambient, before and after freezing.

Starting from +20 °C, both CNT and YP-50 electrodes were still able to utilize most of the surface area (100% for CNT and 86% for YP-50) for EDLC at the medium loading of ca. 3 mg cm^{-2}. The higher utilization in CNT can be explained through deeper electrolyte infiltration facilitated by the more open and larger meso-pores of CNT. While carbon containing smaller pores with larger SSA can lead to higher apparent capacitance, they can also lead to lower material utilization with increased deadweight portion from un-infiltrated pores. Furthermore, the increased tortuosity in the smaller pores of YP-50 can also restrict fast movement of the ions and cause a significantly greater portion of diffusion-limited capacitance than in CNT (i.e. Figs. S1c vs S3c). This will adversely impact the capacitive performance of the carbon electrodes, especially during fast charging/discharging. Nevertheless, there is still a limitation for CNT electrodes in an even higher loading of 6.5 mg cm^{-2}, which was only 76% utilized so that the rest became deadweight without access of the electrolyte solutions during cell fabrication.

At −10 and −20 °C, the ionic conductivity of the Na_2SO_4-PAM-DMSO electrolyte is only about 1 and 0.1% of the values at 20 °C, representing different phases: mostly in liquid phase at −0 °C and completely frozen with some crystal hydrates at −20 °C (Fig. 8). At −10 °C, the bulk of the electrodes can still be highly utilized for up to 3.0 mg cm^{-2} (>90% in CNT and >75% in YP-50 AC). The impact of lower ionic conductivity on Na_2SO_4-PAM-DMSO electrolyte became more apparent when the CNT loading increased to 6.4 mg cm^{-2}, in which only half of the electrodes were utilized. These phenomena were more pronounced at −20 °C, as many of the small pores were blocked by ice and/or crystal hydrates. All the electrodes, except the ones containing <1 mg cm^{-2} loading, became severely limited by the slow ionic conduction and diffusion of ions, as evidenced by the fast decay proportional to $\nu^{0.5}$ (Fig. S6). The significant differences in electrode utilization between −10 °C and −20 °C are more severe on high SSA micro-pore-rich YP-50 AC than that of low SSA meso-pore-rich CNT. In both cases, devices constructed with thinner electrodes can be more tolerant to the freezing of electrolytes and were still functional (with >70% electrode utilization) at −20 °C, which is below the melting point of Na_2SO_4-PAM-DMSO electrolyte.

Using the findings in Fig. 8, the effective utilizable carbon loadings with Na_2SO_4-PAM-DMSO electrolyte in solid cells were established. For CNT, it was 4.8 mg cm^{-2} under ambient, decreasing to ca. 3 and 2.4 mg cm^{-2} at −10 °C and −20 °C respectively. The usable YP-50 AC loading is likely to be at least ca. 2.6 mg cm^{-2} at ambient, decreasing to approximately 2.2 and 1.0 mg cm^{-2} at −10 and −20 °C, respectively. It should be noted that these values are specific to the Na_2SO_4-PAM-DMSO system, and they are probably extremely sensitive to two factors: (i) differences in the ionic conductivities between ambient and low temperatures, and (ii) the viscosity of the precursor solution to form polymer electrolytes. From the perspective of polymer electrolyte development, lowering the viscosity of precursor solution (e.g., by increasing the amount of solvent or employing polymer matrices with lower molecular weight) may be helpful to increase its infiltration into the electrodes. Nonetheless, the framework of this systematic approach can be

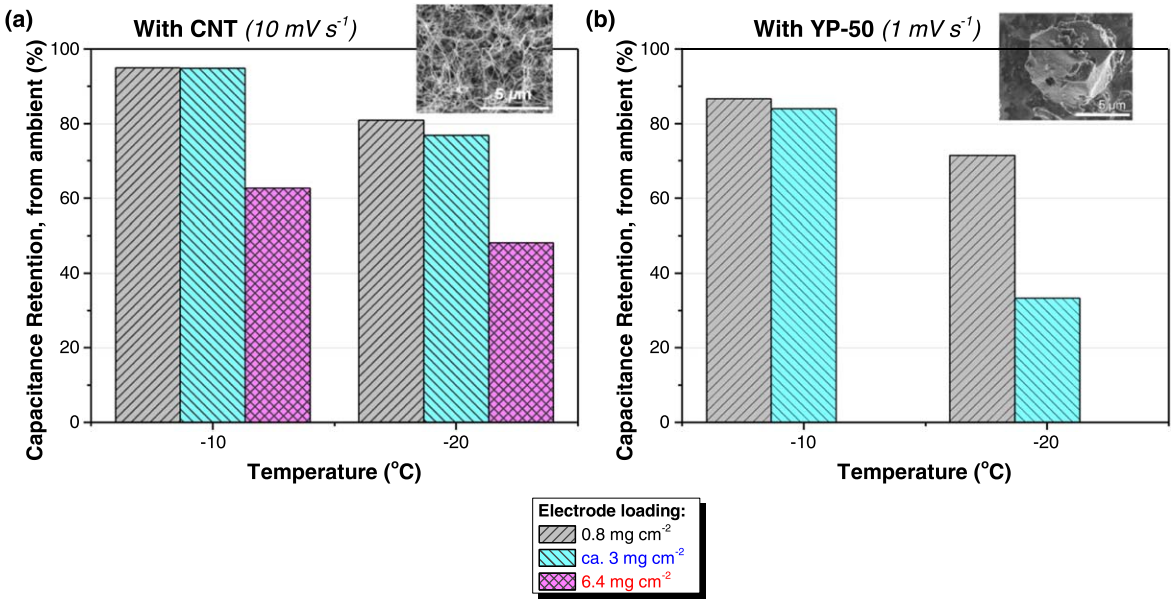

Figure 7. Low temperature capacitance retention (shown as percentage retained from the values at ambient) calculated from (a) CNT cells and (b) YP-50 cells with various electrode loading.

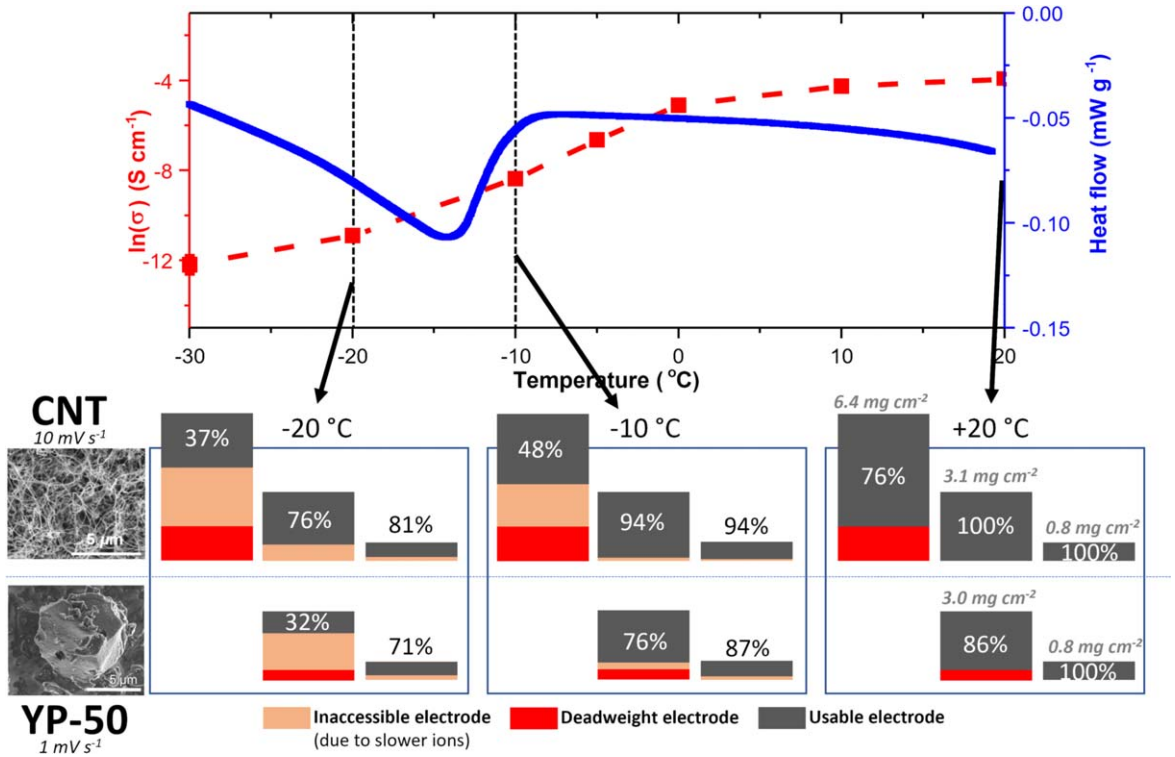

Figure 8. Electrode utilization at various temperatures, correlated to the ionic conductivity and thermal properties of the ternary Na_2SO_4-PAM-DMSO(25,000:1) electrolytes.

applied to aid the design and guide the optimization of solid electrochemical devices with different polymer electrolytes and electrode materials. In general, although thicker electrodes possessing larger amounts of active materials can enhance the cell areal capacitance, they may inflict adverse effects on the rate capability and low temperature performance of the devices, especially to those micro-porous materials.

Conclusions

The performance of solid devices with CNT or YP-50 AC electrodes and Na_2SO_4-PAM-DMSO electrolyte were compared to reveal the effects of carbon loading and porosity on their performance under ambient and low temperatures. Both carbon materials shared similar surface chemistries, but possessed different pore structures (i.e., CNT contains mostly larger meso-pores, whereas YP-50 AC has a larger surface area with mostly smaller micro-pores). In both cases, similar observations were obtained: a thicker electrode with higher carbon loading can increase the areal capacitance but this may not be true for gravimetric capacitance. Leveraging the gravimetric capacitance, the utilizable portion of the electrodes can be estimated. The material utilization in electrodes possessing small and closed pore structures (i.e., YP-50 AC) was lower than those having open mesopores (i.e., CNT) because of the larger portion of inaccessible area in AC electrodes, especially for viscous polymer electrolyte solutions.

At low temperatures, the material utilization is even lower due to the sluggish movement of ions in the electrolyte and poorer electrode/electrolyte interface from pore blockage. The increase in diffusion-limited capacitance will result in a less capacitive profile and poorer rate capability. Although devices constructed with lower carbon loading/thin electrodes have considerably lower deliverable capacitance at ambient temperature, they can still benefit from increased tolerance to the freezing of electrolytes. Also, the optimal electrode thickness can vary significantly depending on the types and pore accessibility of the carbon electrodes. These carbon structures and loading considerations must be accounted for in designing EC cells (liquid and solid) and tailored for their intended applications. Furthermore, the framework developed for comparing material utilization can be used to aid the design and optimization of future generations of solid electrochemical cells with polymer electrolytes.

Acknowledgments

Authors would like to appreciate the financial support from Natural Sciences and Engineering Research Council of Canada (NSERC Discovery Grant RGPIN-2016-06219 and Discovery Grant Supplement 493032). A.V. acknowledges the financial support from Hatch Graduate Scholarship for Sustainable Energy Research (2020) and the University of Toronto Doctoral Completion Award. R.B. is also grateful for the Queen Elizabeth II/Eleanor and Burnett Thall Graduate Scholarship for Science & Technology.

ORCID

Alvin Virya https://orcid.org/0000-0002-2079-3461
Raunaq Bagchi https://orcid.org/0000-0001-6801-663X
Keryn Lian https://orcid.org/0000-0002-2821-1278

References

1. P. Yang and W. Mai, *Nano Energy*, **8**, 274 (2014).
2. D. P. Dubal, N. R. Chodankar, D.-H. Kim, and P. Gomez-Romero, *Chem. Soc. Rev.*, **47**, 2065 (2018).
3. N. A. Choudhury, S. Sampath, and A. K. Shukla, *Energy Environ. Sci.*, **2**, 55 (2009).
4. A. Virya and K. Lian, *Mater. Reports Energy*, **1**, 100005 (2021).
5. J. Li, J. Qiao, and K. Lian, *Energy Storage Mater.*, **24**, 6 (2020).
6. X. Cheng, J. Pan, Y. Zhao, M. Liao, and H. Peng, *Adv. Energy Mater.*, **8**, 1702184 (2018).
7. F. Yu, T. Wang, Z. Wen, and H. Wang, *J. Power Sources*, **364**, 9 (2017).
8. N. Batisse and E. Raymundo-Piñero, *J. Power Sources*, **348**, 168 (2017).
9. A. Virya and K. Lian, *Electrochem. Commun.*, **74**, 33 (2017).
10. X. Zhang, *Adv. Mater. Interfaces*, **2**, 1500267 (2015).
11. M. S. Hong, S. H. Lee, and S. W. Kim, *Electrochem. Solid-State Lett.*, **5**, A227 (2002).
12. Q. Gao, L. Demarconnay, E. Raymundo-Pinero, and F. Beguin, *Energy Environ. Sci.*, **5**, 9611 (2012).
13. E. Frackowiak, Q. Abbas, and F. Béguin, *J. Energy Chem.*, **22**, 226 (2013).

14. A. V. Virya, J. Abella, A. Grindal, and K. Lian, *Batter. Supercaps*, **3**, 194 (2020).
15. A. Balducci, D. Belanger, T. Brousse, J. W. Long, and W. Sugimoto, *J. Electrochem. Soc.*, **164**, A1487 (2017).
16. Y. Chen, Y. Zhang, Z. Lian, Y. Cao, Z. Han, and X. Feng, *npj Flex. Electron.*, **4**, 2 (2020).
17. W. Hou, Q. Liao, S. Xie, Y. Song, and L. Qin, *Coatings*, **12**, 558 (2022).
18. G. Denuault, M. Sosna, and K.-J. Williams, *Handbook of Electrochemistry*, ed. C. G. Zoski (Elsevier, Amsterdam) 1, 431 (2007).
19. J. Zhao and A. F. Burke, *J. Energy Chem.*, **59**, 276 (2021).
20. B. Pal, S. Yang, S. Ramesh, V. Thangadurai, and R. Jose, *Nanoscale Adv.*, **1**, 3807 (2019).
21. W. Ye, H. Wang, J. Ning, Y. Zhong, and Y. Hu, *J. Energy Chem.*, **57**, 219 (2021).
22. J. Zhang and X. S. Zhao, *ChemSusChem*, **5**, 818 (2012).
23. M. K. Jha and C. Subramaniam, *ACS Omega*, **6**, 7970 (2021).
24. X. Wei, X. Jiang, J. Wei, and S. Gao, *Chem. Mater.*, **28**, 445 (2016).
25. M. A. Pope, C. Punckt, and I. A. Aksay, *J. Phys. Chem. C*, **115**, 20326 (2011).
26. K. Breitsprecher, M. Janssen, P. Srimuk, B. L. Mehdi, V. Presser, C. Holm, and S. Kondrat, *Nat. Commun.*, **11**, 6085 (2020).
27. H. Wu, M. Genovese, K. Ton, and K. Lian, *J. Electrochem. Soc.*, **166**, A821 (2019).
28. B. Yao et al., *Nano Lett.*, **21**, 3731 (2021).
29. N. R. Chodankar et al., *J. Mater. Chem. A*, **9**, 26603 (2021).
30. A. Virya, R. Bagchi, and K. Lian, *Electrochim. Acta*, **376**, 137984 (2021).
31. Y. H. Hu and E. Ruckenstein, *Ind. Eng. Chem. Res.*, **43**, 708 (2004).
32. S. Ozden et al., *Carbon*, **119**, 142 (2017).
33. H. Gao, A. Virya, and K. Lian, *Electrochim. Acta*, **138**, 240 (2014).
34. M. Genovese, H. Wu, A. Virya, J. Li, P. Shen, and K. Lian, *Electrochim. Acta*, **273**, 392 (2018).
35. P. L. Taberna, P. Simon, and J. F. Fauvarque, *J. Electrochem. Soc.*, **150**, A292 (2003).
36. S. Ardizzone, G. Fregonara, and S. Trasatti, *Electrochim. Acta*, **35**, 263 (1990).